RESEARCH ARTICLE

Check for updates

Distance produces beauty? regulating the distance of Fe atomic pairs to enhance electrocatalytic CO₂ reduction†

Xiaofei Wei, Huakai Xu, Chuanhai Jiang, Zhifei Wang, Yuguo Ouyang, Chunyu Lu, Yuan Jing, Shiwei Yao, Xiaoqing Lu [ID] and Fangna Dai [ID] *

Metal atom dispersed catalysts with high catalytic activity and accurate active sites are considered as promising catalyst materials for electrocatalytic CO_2 reduction reactions (CO_2RRs). Electronic structure regulation of active sites is a crucial means to improve the catalytic performance. Hence, Fe atom catalysts (FeN_4-Dx (x = 1, 2, 3, and 4)) with pairs of Fe atoms at different distances were constructed and the effect of distance on the catalytic performance was further investigated. Based on the structural stability and the activation effect for CO_2, the FeN_4-D1 structure (D1 = 2.39 Å) exhibited good CO_2RR selectivity and catalytic activity for producing CO. Moreover, due to the double active sites of Fe atomic pairs, the FeN_4-D1 structure had superior catalytic performance and selectivity for the CO_2RR to ethanol by the *CO−*CHO coupling with low reaction free energy. Combined with detailed calculations of the electronic structure, a suitable distance of Fe atomic pairs regulated the d-band center of active sites, which modified the interaction between the FeN_4-D1 structure and *CO intermediates and promoted the C−C coupling process. Therefore, the FeN_4-D1 structure can be used as a promising electrocatalyst for the CO_2RR to C_2 products and the accurate regulation method of active sites may provide new ideas for the design of efficient catalysts.

1. Introduction

Electrocatalytic CO_2 reduction reaction (CO_2RR) is an effective method to mitigate the greenhouse effect and promote the conversion of carbon into value-added chemicals.[1–4] On the basis of high metal atom utilization rate and easily regulated active sites, atom-dispersed catalysts have broad application prospects in the CO_2RR.[2,5–7] Further, several means have been used to further improve the catalytic activity of the active sites, such as structural defects,[8,9] introducing heteroatoms,[10–12] axial coordination,[13–15] bimetallic centers,[16–18] and regulating the distance of the active sites.[19,20] However, the distance effect of the active sites on the catalytic performance of atom-dispersed catalysts for the CO_2RR is rarely reported. The double active sites of catalysts have two adsorption positions for the reaction intermediates, which may facilitate C−C coupling to proceed and C_2 products to form in the CO_2RR. Therefore, investigating the distance effect of the active sites on the

catalytic performance of atom-dispersed catalysts is of great significance for enhancing CO_2 catalytic conversion.

Generally, Cu-based materials are considered as effective catalysts for the CO_2RR to multi-carbon products;[21–24] however, their poor product selectivity and weak interaction with CO_2 inhibit the activity for electrochemical CO_2 reduction.[24–26] Recently, Fe atom catalysts have been found to exhibit outstanding electrocatalytic activity in the CO_2RR.[5,6,12,14,27] Due to the stable adsorption interaction between CO_2 molecules and Fe active sites, the reaction free energy of initial CO_2 hydrogenation on the surface of Fe atom catalysts can be reduced. In addition, regulating the adsorption of key intermediates on Fe-based catalysts was an effective way to facilitate the C−C coupling process and the conversion of CO_2RR to C_2 products.[27–29] The Fe-n-f-CNT single-atom catalyst synthesized by Hwang *et al.* exhibited superior electrocatalytic performance for the CO_2RR to ethanol with 45% faradaic efficiency.[27] Moreover, An *et al.* designed a hybrid Fe−B dual-atom center to facilitate C−C coupling of low free energy barrier by enhancing the spin state of Fe, which proved that Fe sites had the potential of producing C_2 products in the CO_2RR process.[29] Considering the size effect, single-atom catalysts can exhibit unique product selectivity.[7,30–32] And regulating the distance of active sites may further improve the catalytic activity.[19,20] Yu *et al.* synthesized

School of Materials Science and Engineering, China University of Petroleum, Qingdao, Shandong 266580, P. R. China. E-mail: fndai@upc.edu.cn

FeN4 single-atom catalysts with accurate structural control and found that the Fe atomic sites at a specific distance could exhibit strong oxygen reduction reaction activity by regulating the filling of occupied d orbitals of Fe sites.[20] However, the electrocatalytic activity for the CO_2RR on Fe atomic pair sites is rarely reported and the intrinsic mechanism of electronic structure regulation in Fe atomic pairs is not clear. Combining the superior adsorption and activity of Fe single atoms on CO_2, Fe atomic pairs may also exhibit good performance in the C–C coupling process. Therefore, catalyst materials with high electrocatalytic activity and product selectivity can be designed by adjusting the electronic structure between Fe atomic pair active sites, which is of great significance to promote the development of the CO_2RR.

Hence, in this work, FeN_4-Dx (x = 1, 2, 3, and 4) structures of four Fe atomic pairs at different distances were designed, and the effect of distance on their electrocatalytic performance in the CO_2RR was investigated by density functional theory (DFT). Firstly, the structural stability of the four catalysts was analyzed from the perspectives of geometrical structure, electronic structure, thermodynamics, and electrochemistry by calculating geometric optimization, bonding interaction, formation energy, and dissolution potential, respectively. To analyze the initial catalytic activity of the four Fe atom pairs on CO_2, the adsorption and activation of CO_2 were calculated and compared in detail. Subsequently, the catalytic performance of FeN_4-Dx structures on the CO_2RR was further investigated, including the free energy of potential limiting steps and the comparison of the CO_2RR with side reactions. On the basis of double active sites, the C–C coupling process was calculated and possible C_2 products in the CO_2RR were analyzed. Finally, the electronic structure of the key intermediates was analyzed in detail, and the effect of distance on the electrocatalytic performance of the CO_2RR was discussed.

2. Computational method

All calculations in this work were performed by spin-polarized density functional theory (DFT) in Vienna Ab initio Simulation Package (VASP) 6.1.1.[33] Projector augmented wave (PAW) and Perdew–Burke–Ernzerhof (PBE) generalized gradient approximation (GGA) were used to describe the ion–electron interaction and electronic exchange–correlation energy, respectively.[34] The plane wave cutoff energy was set as 450 eV. K-Point meshes of $3 \times 3 \times 1$ and high-density $15 \times 15 \times 5$ were used to optimize geometry structures and accurately analyze electronic structures such as Bader charge transfer, charge difference density, and density of states (DOS).[35] The electronic energy and the force of catalysts converged to 1.0×10^{-5} eV per atom and 0.02 eV Å^{-1}, respectively. The lattice parameters of FeN_4-Dx structures were as follows: a = 14.76 Å, b = 12.78 Å, and $\alpha = \beta = \gamma = 90°$. Besides, in order to minimize the interactions of repeated slabs, a vacuum space of 15 Å was constructed along the c-axis. And the Grimme (DFT+D3) method was performed to correct the van der Waals interactions. Considering the solvent

effect of water, the VASPsol package was used to build an implicit solvent model.[36]

Generally, the adsorption energy (E_{ads}) between catalysts and adsorbates can be calculated by the following formula:

$$E_{ads} = E_{*a} - E_* - E_a \qquad (1)$$

where E_{*a}, E_*, and E_a represent the total energy of the system, the energy of the catalyst structures, and the energy of the adsorbates, respectively.

Charge density difference ($\Delta\rho$) can be used to analyze the electron transfer direction after the interaction between two fragments (A and B), which can be calculated by

$$\Delta\rho = \rho_{AB} - \rho_A - \rho_B \qquad (2)$$

And the plane-averaged electron density difference along the z axis ($\Delta\rho(z)^{avg}$) is described as follows:[37]

$$\Delta\rho^{avg}(z) = \int \sum(z) dx dy \, \Delta\rho = \sum_{ij} \Delta x_i \Delta y_j \Delta\rho_{i,j} \qquad (3)$$

where the z axis is along the c-axis lattice of the structural model and x/y is the cross-section of the x–y plane at z, and i and j are the one-point divided lattice axis and b-axis lattice, respectively.

The calculation of reaction free energy was based on the computational hydrogen electrode (CHE) model.[38] And the values of the reaction free energy difference (ΔG) can be obtained by the following formula:

$$\Delta G = \Delta E + \Delta E_{ZPE} + \int C_p dT - T\Delta S \qquad (4)$$

where ΔE is the energy change calculated by DFT. ΔE_{ZPE} is the zero-point energy correction. $\int C_p dT$ and ΔS are the enthalpic temperature correction and the reaction entropy change at room temperature (T = 298.15 K), respectively. Specifically, the saturated vapor pressure of 0.035, 0.053, 0.166, and 0.077 atm was employed for H_2O, $HCOOH$, CH_3OH, and C_2H_5OH, respectively. And VASPKIT software was used to post-process the relevant results.[39]

3. Results and discussion

3.1 Structure stabilities

To investigate the distance effect of metal atomic pairs on electrocatalytic CO_2 reduction, four typical structures (FeN_4-Dx, x = 1, 2, 3, and 4) containing double FeN_4 active sites were constructed in this work. And every Fe metal site was anchored by four nitrogen atoms to ensure its same coordination environment. The optimized structural models of FeN_4-Dx (x = 1–4) are displayed in Fig. 1a–d, in which the distances of Fe atomic pairs were 2.39, 4.14, 6.53, and 8.62 Å, respectively. Four FeN_4-Dx structures all had no obvious bending deformation in the geometry optimization. The detailed structural parameters are summarized in Table S1 (ESI†) and the Fe–N bond average lengths were between 1.87 Å and 1.91 Å. Further, charge density difference between the metal atom and nitrogen-doped carbon and corresponding Bader charge transfer indicated
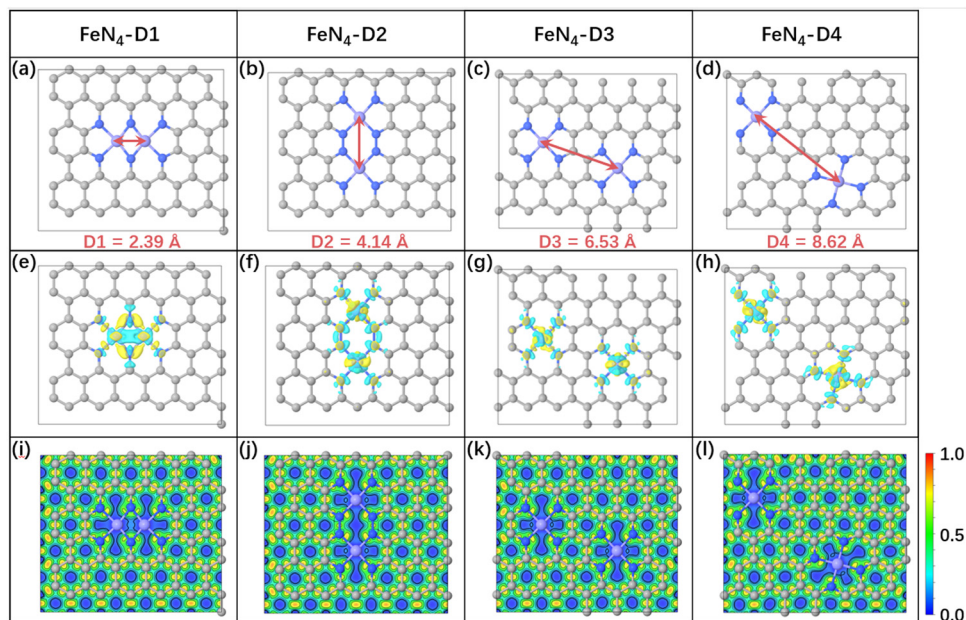
Fig. 1 The optimized structures of four different Fe atomic pairs (a–d), charge density difference between metal atoms and nitrogen-doped carbon (e–h) (the regions in yellow and cyan represent, respectively, electron accumulation and deletion. The isosurface levels are 0.01 e bohr^{-3}) and the corresponding electron localization function (i–l).

that Fe atomic pairs transferred electrons to adjacent nitrogen atoms, which can be anchored stably by coordinated pyridine nitrogen atoms (Table S1, ESI† and Fig. 1e–h). Based on the distance effect of the Fe atomic pairs, the magnetic moments and d-band centers of the four catalysts in Table S1 (ESI†) were different from each other, which may change the catalytic properties of Fe atom catalysts. According to the analysis of electron localization function in Fig. 1i–l, there is an obvious concentrated distribution of electrons in Fe–N bonds, indicating that Fe metal atoms have relatively strong electronic interaction with doped nitrogen. Moreover, projected density of states (PDOS) between Fe-3d and N-2p was used to analyze further their valence orbital interaction (Fig. S1, ESI†). Notably, Fe-3d orbitals in the four FeN$_4$-Dx structures have good orbital overlapping with N-2p near the Fermi level, which indicates that the different distance Fe atomic pairs anchored by pyridine nitrogen atoms have great structural stability in the electronic structures.

Formation energy (E_f) and dissolution potential (U_{diss}) are used to evaluate structural stability in thermodynamics and electrochemistry, which can be calculated as follows: $E_f = (E_{total} - E_{NC} - E_{Fe} \times 2)/2$ and $U_{diss} = U^0 - E_f/ne$, respectively. E_{total}, E_{NC}, and E_{Fe} represent the energies of the total FeN$_4$-Dx system, metal free nitrogen-doped carbon material, and Fe metal atom, respectively. U^0 and n are, respectively, the standard dissolution potential of bulk metal and the number of electrons transferred during the dissolution of the metal atom. As can be seen from Fig. S2 (ESI†), FeN$_4$-Dx structures have negative E_f values (from −9.29 eV to −7.21 eV) and positive U_{diss} values of 3.16–4.20 V, which ensures that FeN$_4$-Dx structures have stable thermodynamic and electrochemical stability, respectively. Combined with previous reports,[20] FeN$_4$-Dx structures containing

different distance metal atomic pairs have great potential to be synthesized and applied in electrocatalysis. Therefore, the distance effect of Fe atomic pairs might also enhance the performance of electrocatalytic CO$_2$ reduction reaction, which can be further investigated in detail.

3.2 Initial CO$_2$ adsorption and activation

In general, the initial adsorption and activation of CO$_2$ molecules on electrocatalysts is considered as the first step in the CO$_2$ reduction reaction process, which is closely related to the catalytic activity of the electrocatalyst. The optimized CO$_2$ adsorption structures and structural parameters of the four FeN$_4$-Dx catalysts are summarized in Table S2 (ESI†). The C–Fe bond lengths between CO$_2$ and active sites ranged from 2.02 to 2.11 Å and the bond angles of O–C–O were activated to bend (132.99°–137.75°) after CO$_2$ adsorbed on the four FeN$_4$-Dx structures. Obvious structural deformation indicated that CO$_2$ molecules can be efficiently activated by Fe atomic pairs and exhibit stable chemisorption on metal centers. Furtherly, Bader charge transfer and charge density difference of CO$_2$ adsorption structures were calculated to analyze the interaction between CO$_2$ molecules and metal centers (Fig. 2). As shown in Fig. 2, according to the Bader charge transfer, Fe metal centers mainly acted as electron donors, while CO$_2$ accepted most electrons to be activated. Charge density difference distribution and the corresponding profile map indicated that CO$_2$ can be adsorbed stably on FeN$_4$-Dx structures by strong C–Fe bond interaction. Moreover, the adsorption energies of CO$_2$ on FeN$_4$-Dx structures also indicated that Fe metal centers had a stable adsorption interaction with CO$_2$ (Table S2, ESI†). Partial density of states (PDOS) in Fig. S3 (ESI†) showed the valence
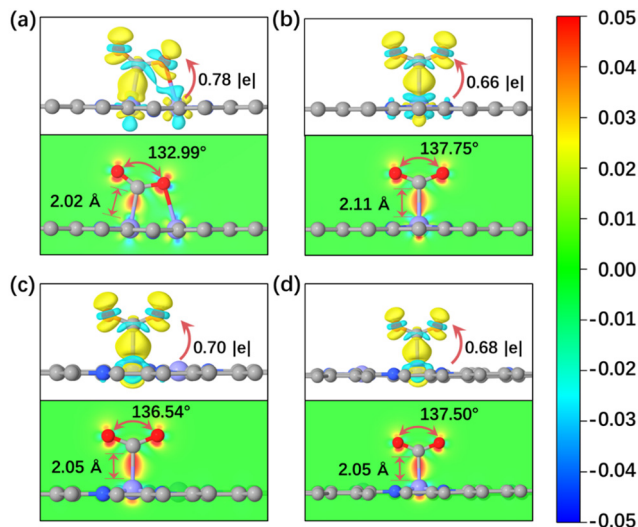
Fig. 2 (a–d) Charge density difference and Bader charge transfer of CO_2 adsorbed on FeN_4-Dx (x = 1, 2, 3, and 4) (the regions in yellow and cyan represent, respectively, electron accumulation and deletion. The isosurface levels are 0.005 e bohr^{-3}).

orbital electron interaction between the Fe 3d-orbital of active sites and CO_2 2p-orbital. The orbital overlapping between Fe-3d and CO_2-2p orbitals near the Fermi level further proved that the four types of Fe active sites all had good interaction with CO_2 molecules. Obvious bending deformation of CO_2 molecules on the four types of atomic pairs proved that different distance metal centers all had catalytic potential in the CO_2RR. Specifically, CO_2 was adsorbed on the bridge sites of the FeN_4-D1 structure due to its close Fe pair sites. And the stable adsorption configuration showed that CO_2 was more easily activated and adsorbed on FeN_4-D1 than on the top sites of other FeN_4-Dx structures. In addition, the values of the Bader charge transfer between CO_2 molecules and FeN_4-Dx structures show a similar trend with the change of CO_2 bond angles (Table S2, ESI†). Therefore, the special Fe pair sites of the FeN_4-D1 structure may have an advantage in promoting the initial CO_2 adsorption and activation.

3.3 CO_2RR to C_1 products and HER side reactions

Every elementary reaction of the CO_2RR after CO_2 adsorption and activation is an important factor to analyze the catalytic reduction performance of electrocatalysts. Generally, the initial CO_2 reduction steps can be divided into two hydrogenation reactions: hydrogen protons attacking oxygen atoms (*CO_2 + H^+ + e^- → *COOH) and hydrogen protons attacking carbon atoms (*CO_2 + H^+ + e^- → *HCOO). Different reduction products can be produced by different reaction pathways, depending on intermediates with relatively low reaction free energy. As for the CO product, CO_2 prefers to undergo this reduction process: CO_2 → *CO_2 → *COOH → *CO → CO. As shown in Fig. 3a, the reaction free energies (ΔG) of the CO_2RR to CO on FeN_4-Dx (x = 1, 2, 3, and 4) structures were compared and the ΔG values of critical steps were labeled. Obviously, the potential limiting step (PLS) of the CO_2RR to CO on FeN_4-D1 was the formation of the

COOH intermediate (CO_2 + H^+ + e^- → *COOH, ΔG = 0.31 eV). As for FeN_4-D2, FeN_4-D3, and FeN_4-D4 structures, the CO desorption was the PLS. The high reaction free energy of the CO desorption on FeN_4-D2, FeN_4-D3, and FeN_4-D4 structures indicated that the Fe atomic pair sites with long distance had powerful adsorption for CO and inhibited CO desorption. The PLS ΔG value of 0.31 eV on FeN_4-D1 was much lower than those on FeN_4-D2 (ΔG = 1.32 eV), FeN_4-D3 (ΔG = 1.26 eV), and FeN_4-D4 (ΔG = 1.17 eV) structures, which showed that FeN_4-D1 had the superior catalytic performance in the CO_2RR to CO compared to other catalyst structures. Formic acid (HCOOH), as another two-electron reduction product, had two reaction pathways: Path 1: CO_2 → *CO_2 → *COOH → *HCOOH → HCOOH, and Path 2: CO_2 → *CO_2 → *HCOO → *HCOOH → HCOOH. By comparing the free energy of the two reaction pathways and choosing the more favorable reaction process, the free energy profile of producing HCOOH on the four catalysts was compared and analyzed. As can be seen in Fig. 3b, FeN_4-D1, FeN_4-D3, and FeN_4-D4 structures followed Path 1 to reduce CO_2 to HCOOH, while FeN_4-D2 preferred to follow Path 2. And the PLS of forming HCOOH on the four catalysts was also different to some extent due to the distance difference of Fe atomic pair sites. By comparing the ΔG values of the PLS, the FeN_4-D3 structure was more advantageous than other catalysts in the CO_2RR to HCOOH, and its ΔG value was only 0.22 eV. Therefore, FeN_4-D3 with specific distance (6.53 Å) Fe pair sites had superior catalytic performance in producing formic acid compared to other catalyst structures.

It's worth noting that the hydrogen evolution reaction (HER) is considered to be the main side reaction for electrocatalytic CO_2 reduction, which inhibits the CO_2RR process. Fig. 3c shows the reaction free energy of the HER on the four catalysts. On the basis of the high ΔG value of 0.33 eV, the FeN_4-D1 structure had a better inhibition effect on the HER than the other three catalyst structures, which was conducive to promoting the catalytic reduction of CO_2. Moreover, the selectivity of FeN_4-Dx (x = 1, 2, 3, and 4) structures between the HER and CO_2RR was further investigated by comparing the ΔG values of first electron transfer proton coupling (Fig. 3d). The ΔG values of forming *COOH intermediates on the four catalyst structures were below the dotted line, which indicated that they all had good CO_2RR selectivity. Therefore, the Fe atomic pair sites in FeN_4-Dx (x = 1, 2, 3, and 4) structures were worthy to further investigate their catalytic performance in the CO_2RR. Considering the stable adsorption of CO on FeN_4-Dx (x = 1, 2, 3, and 4) catalysts, the multi-electron reduction products of the CO_2RR, such as methanol (CH_3OH) and methane (CH_4), were further compared and analyzed. On the basis of reaction free energy of different intermediates in Table S3 (ESI†), the optimal reaction pathways of the CO_2RR to CH_3OH and CH_4 on the four catalysts are summarized in Fig. 3e and f, respectively. Based on the linear scaling relations,[40,41] the stable adsorption interaction between *CO intermediates and FeN_4-Dx (x = 2, 3, and 4) structures resulting in the *CO hydrogenation (*CO + H^+ + e^- → *CHO) was still the rate-determining step of multi-electron C_1 reduction products. And the ΔG values of the PLS were as follows: FeN_4-D3 (ΔG = 0.73 eV) > FeN_4-D4
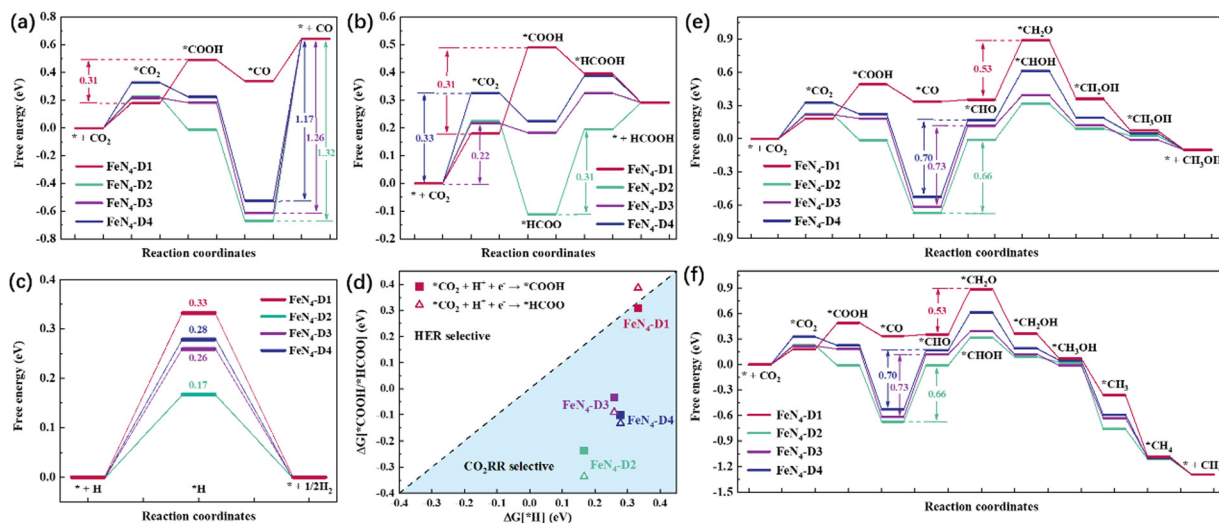
Fig. 3 Reaction free energy profile of CO_2 reduction to CO (a) and HCOOH (b). HER free energy profile (c) and the comparison between the HER and CO_2RR on the four catalysts (d). Reaction free energy profile of the CO_2RR to CH_3OH (e) and CH_4 (f) on FeN_4-Dx (x = 1, 2, 3, and 4) structures.

($\Delta G = 0.70$ eV) > FeN_4-D2 ($\Delta G = 0.66$ eV). Specifically, the FeN_4-D1 structure had a different rate-determining step with other

catalysts. The hydrogenation of *CHO to *CH_2O ($\Delta G = 0.53$ eV) on the FeN_4-D1 structure played the controlling role of producing
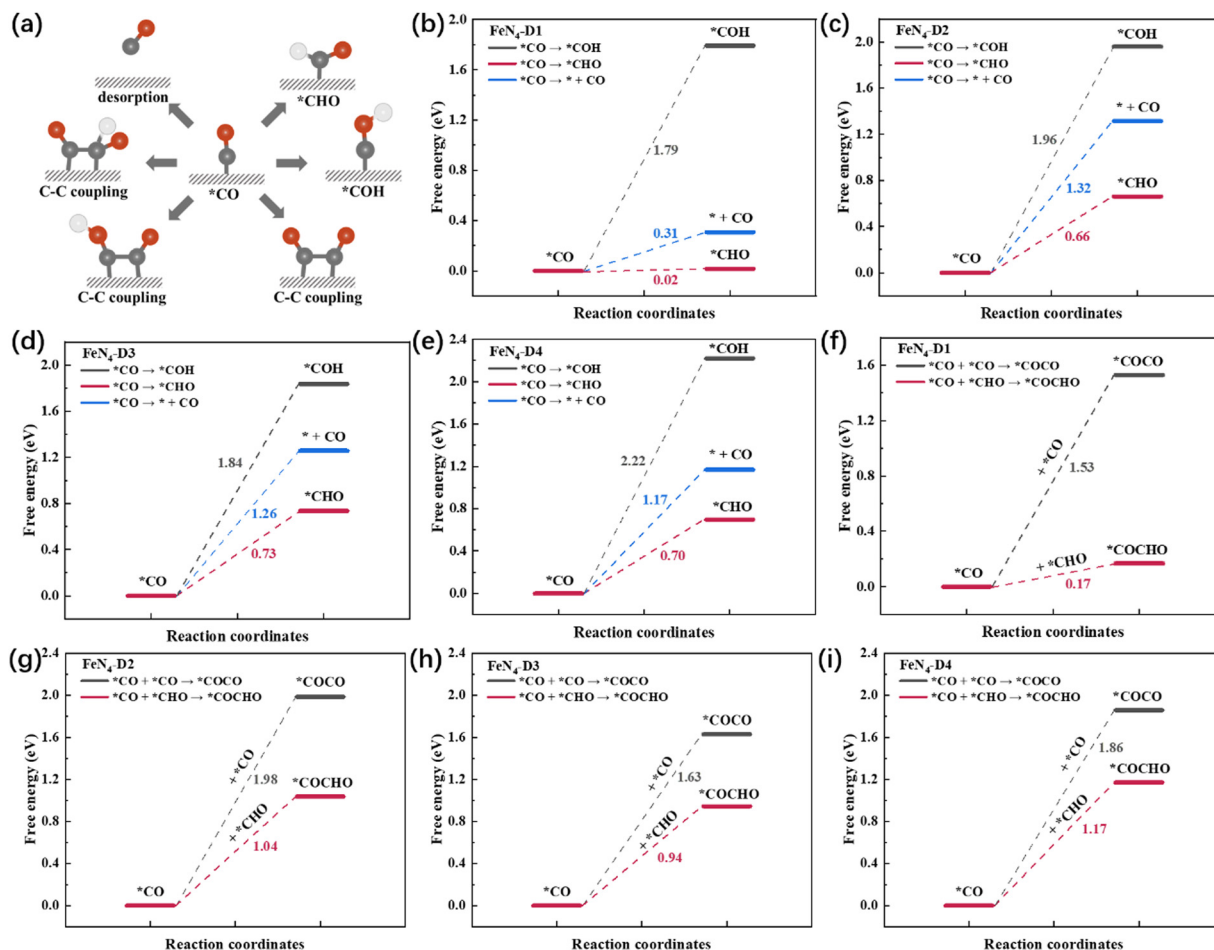

Fig. 4 (a) Schematic diagram of different reaction pathways of the *CO intermediate. (b–e) Free energy profile of CO desorption and *CO hydrogenation. (f–i) Comparison of C–C coupling on four FeN_4-Dx (x = 1, 2, 3, and 4) structures.

CH_3OH thermodynamically. It's worth noting that there were similar reaction intermediates before $*CH_3OH$ in the formation of CH_3OH and CH_4. Hence, the two reduction products would have the same PLS in the whole reaction process. Limiting potential (U_L, V) can be obtained by the ΔG values of the PLS: $U_L = -\Delta G_{max}/e$. As shown in Fig. S4 (ESI†), the FeN_4-D1 structure exhibited superior potential for the CO_2RR to CO and multielectron C_1 reduction products, and the FeN_4-D3 structure had the optimal U_L values on producing HCOOH in the four catalysts. In a word, adjusting the distance of Fe atomic pair sites has an important regulatory effect on the electrocatalytic performance. Moreover, two active sites of Fe atomic pairs have the potential to promote deep CO_2 reduction.

3.4 *CO intermediate analysis and C–C coupling

*CO was a key intermediate in the CO_2RR process, participating in many possible reaction pathways such as CO desorption, two hydrogenation models, and three types of C–C coupling (Fig. 4a). In order to screen the optimal reaction pathway of *CO intermediate on the four catalysts, reaction free energies of different pathways were calculated and are compared in Fig. 4b–i. Firstly, compared with CO desorption and *CO hydrogenation to *COH, *CO intermediates were prone to form *CHO intermediates with the lowest ΔG pathway on the four FeN_4-Dx (x = 1, 2, 3, and 4) structures (Fig. 4b–e). Therefore, the multi-electron reduction products might occupy a dominant position in the CO_2RR process. Generally, C_2 products have three types of C–C coupling: *CO–CO, *CO–*COH, and *CO–*CHO coupling. Due to the high ΔG of *CO hydrogenation to

*COH intermediates, *CO–*COH coupling was not considered when comparing the optimal coupling model of the CO_2RR process. As shown in Fig. 4f–i, the free energies of *CO–CO coupling and *CO–*CHO coupling on the four catalysts were calculated, respectively. Obviously, *CO–*CHO coupling exhibited the superior advantage of lower ΔG values than *CO–CO coupling, which indicated that *CO–*CHO coupling might be the main C–C coupling mode on Fe atom dispersed catalysts with Fe pair sites. What's more, the *CO–CHO coupling on the FeN_4-D1 structure had the lowest free energy (ΔG = 0.17 eV) among the four catalysts, which indicated that the FeN_4-D1 structure had more potential to produce C_2 products in the CO_2RR process. The close Fe pair sites might also play an important role in reducing the energy required for the migration of critical intermediates. The ΔG values of *CO–CHO coupling on FeN_4-D2, FeN_4-D3, and FeN_4-D4 catalysts were, respectively, 1.04, 0.94, and 1.17 eV. Thus, the high C-C coupling free energy may be the main reason that Fe single atom catalysts have a poor catalytic performance for the CO_2RR to C_2 products. To sum up, precisely controlling the distance of Fe atomic pair sites may greatly improve their catalytic performance in the CO_2RR.

To investigate the catalytic performance of the FeN_4-D1 catalyst on the CO_2RR to C_2 products, the reaction free energies of C_2H_4 and C_2H_5OH were calculated (Table S4, ESI†) and the optimal reaction pathways are displayed in Fig. 5a. It can be seen that the endothermic process *CHOCHOH + H$^+$ + e$^-$ → *CHOCH + H_2O (ΔG = 0.34 eV) was the key limiting step in producing C_2 products. And the key ΔG values of C_2H_4 and
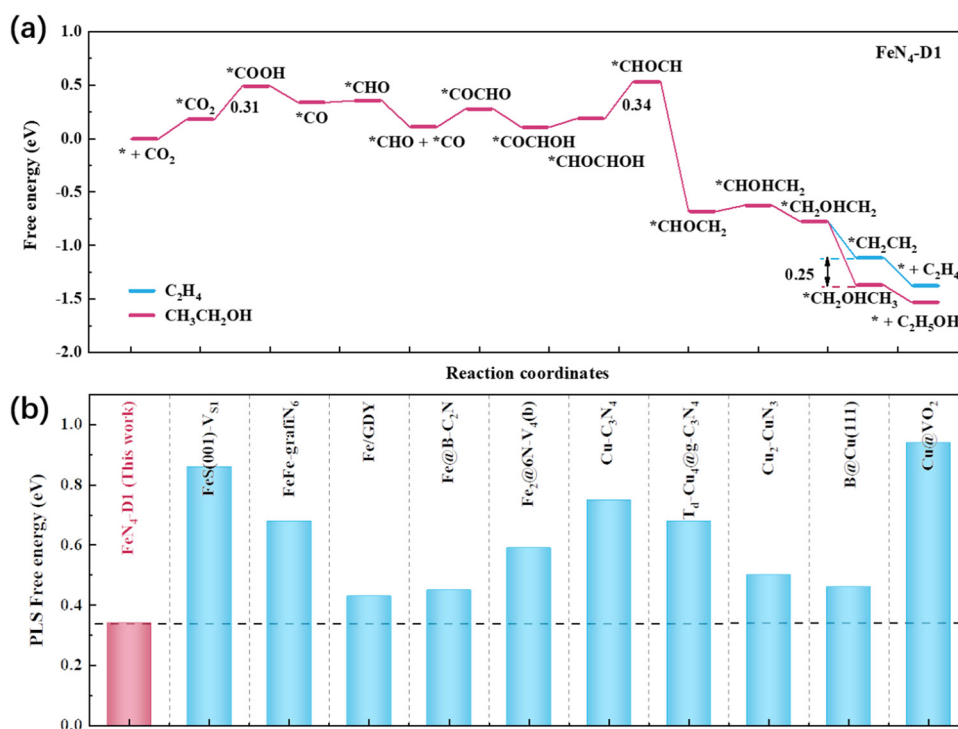

Fig. 5 (a) Reaction free energy profile of CO_2 reduction to C_2H_4 and C_2H_5OH on the FeN_4-D1 structure. (b) Comparison of the FeN_4-D1 structure with some reported catalysts on the PLS free energy of C_2H_5OH.

C_2H_5OH were much lower than those of CH_3OH and CH_4, indicating that the FeN_4-D1 structure was more inclined to deeply reduce CO_2 to C_2 products when *CO intermediates were formed. Moreover, the *CH_2OHCH_2 intermediate was a watershed between C_2H_4 and C_2H_5OH, which had two hydrogenation methods to form *CH_2CH_2 and *CH_2OHCH_3, respectively, with endothermic reaction. The Boltzmann distribution formula $\exp[-(\Delta G)/(k_BT)]$ can be used to estimate the selectivity of two pathways based on their free energy difference.[28,42,43] *CH_2OHCH_3 intermediates were more readily available than *CH_2CH_2, with a free energy difference of about 0.25 eV. Thus, $\Delta G = -0.25$ eV, $T = 298.15$ K, and the molar ratio between C_2H_5OH and C_2H_4 was about $(1.68 \times 10^4):1$, which indicated that the FeN_4-D1 structure showed a better product selectivity toward C_2H_5OH than C_2H_4 in the CO_2RR. In order to highlight the catalytic performance of the FeN_4-D1 structure on the CO_2RR to C_2H_5OH, some reported catalysts were summarized and compared (Fig. 5b and Table S5, ESI†).[23,24,28,29,44–49] Compared with usual Cu catalysts and iron-containing catalysts, the FeN_4-D1 structure with specific distance Fe atomic pair sites exhibited more competitive catalytic performance for the CO_2RR to ethanol. Therefore, the FeN_4-D1 structure can be used as a promising electrochemical catalyst for producing ethanol.

3.5 Electronic structure analysis of *CO intermediates

The FeN_4-D1 structure had the superior catalytic performance on the CO_2RR to ethanol, which can be attributed to the mild interaction between the key reaction intermediates and Fe atomic pair active sites with a specific distance (2.39 Å). *CO intermediates were important components in the C–C coupling process and played a pivotal role in the selectivity to C_1 and C_2 products. Therefore, the detailed electronic structures of *CO intermediates on the four different distance Fe pair sites were calculated and analyzed, and the nature of the catalytic reaction mechanism was further investigated. Fig. 6a–d shows the charge density difference between *CO intermediates and catalysts. To visualize the distribution of electron density intuitively, plane-averaged electron density difference along the z axis ($\Delta\rho(z)^{avg}$, e Å^{-1}) was drawn together as well. It can
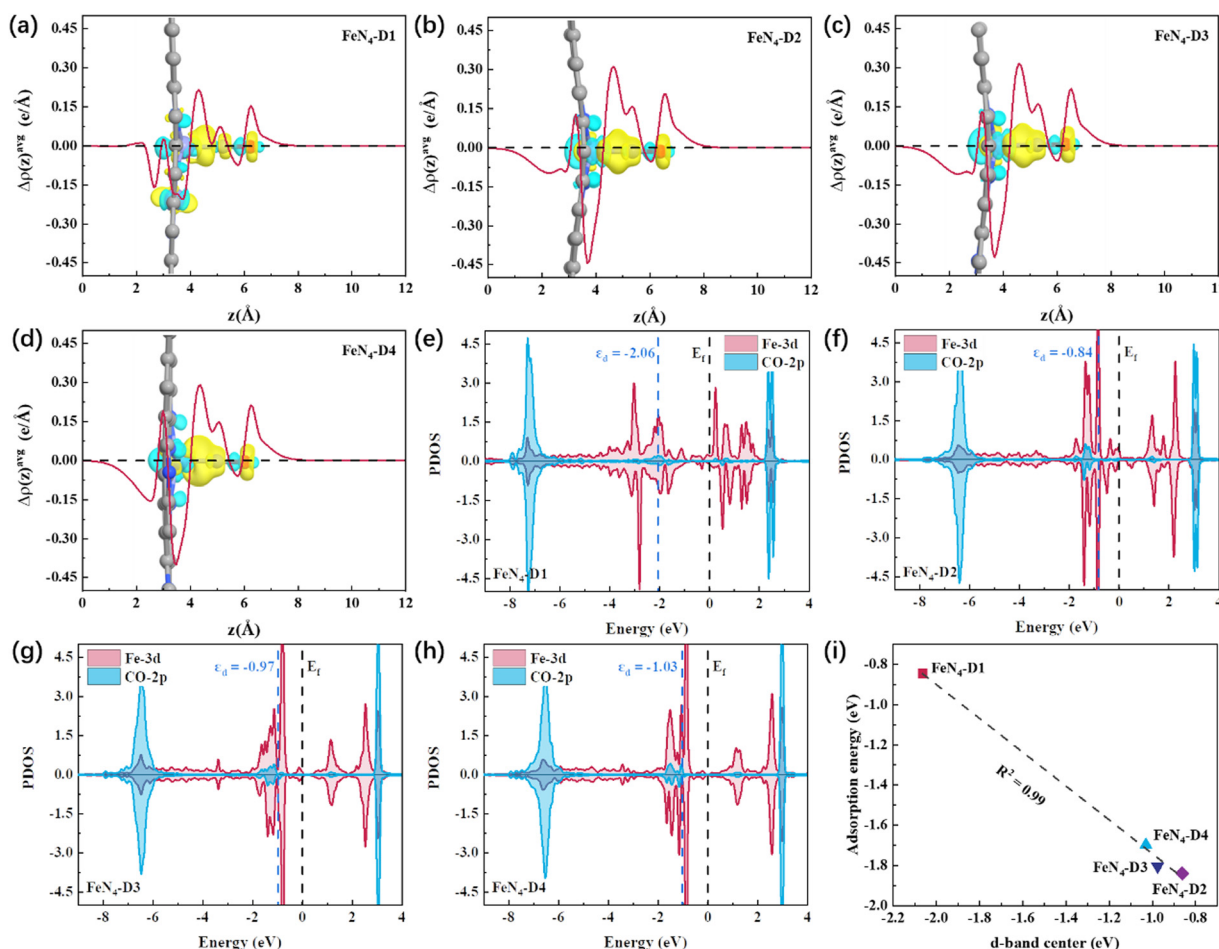

Fig. 6 (a–d) Charge density difference and the corresponding plane-averaged electron density difference along the z axis of *CO intermediates adsorbed on FeN_4-Dx ($x = 1$, 2, 3, and 4) structures (the regions in yellow and cyan represent, respectively, electron accumulation and deletion. The isosurface levels are 0.005 e bohr^{-3}). (e–h) Partial density of states (PDOS) between the 2p-obital of CO and 3d-orbital of adsorbed Fe sites on the four catalysts, respectively. (i) The relationship between the d-band center (ε_d) of adsorbed Fe sites and the adsorption energy of *CO intermediates.

be observed in Fig. 6a–d that a large number of electrons were concentrated on the C–Fe bonds between Fe atom active sites and *CO intermediates. Among them, the charge density concentration region of the *CO intermediate adsorbed on the FeN$_4$-D1 structure was weaker than that of other catalysts. And the curve of z axis plane-averaged electron density difference also indicated that the *CO intermediate adsorbed on the FeN$_4$-D1 structure had the lowest $\Delta\rho(z)^{avg}$ peak (4 Å < z < 6 Å) in the four *CO intermediate adsorption configurations. Therefore, low charge density distribution of C–Fe bonds may weaken the interaction between *CO intermediates and the FeN$_4$-D1 structure. Furtherly, partial density of states (PDOS) between the 2p-orbital of CO and 3d-orbital of adsorbed Fe sites was calculated to analyze their valence shell electron interaction (Fig. 6e–h). It was obvious that the overlapping region between CO-2p and Fe-3d orbitals of the FeN$_4$-D1 structure below the Fermi level was the smallest among the four FeN$_4$-Dx catalysts. Moreover, the antibonding orbitals formed by *CO with FeN$_4$-Dx (x = 2, 3, and 4) were all higher than those formed by *CO with the FeN$_4$-D1 catalyst, which enhanced the electronic interaction between *CO and FeN$_4$-Dx (x = 2, 3, and 4) catalysts. The d-band center (ε_d) of metal active sites can serve as a descriptor to compare the adsorption interaction.[50] It is worth noting that Fe active sites of the FeN$_4$-D1 catalyst had the lowest d-band center position far away from the Fermi level. And the ε_d values of the four catalysts followed FeN$_4$-D2 ($\varepsilon_d = -0.84$) > FeN$_4$-D3 ($\varepsilon_d = -0.97$) > FeN$_4$-D4 ($\varepsilon_d = -1.03$) > FeN$_4$-D1 ($\varepsilon_d = -2.06$). Fig. 6i displays the relationship between the ε_d values and *CO intermediate adsorption energy. Obviously, the adsorption energies of *CO intermediates were linearly correlated with the d-band center of Fe active sites. The FeN$_4$-D1 catalyst had the weak interaction with *CO intermediates based on its low d-band center. Therefore, the appropriate distance of Fe atom pairs modulated the d-band center of active sites, which adjusted the interaction between key intermediates and catalysts, and promoted the catalytic performance of the CO$_2$RR.

4. Conclusions

In this work, different distance Fe atomic pairs were anchored by pyridine nitrogen to construct four FeN$_4$-Dx (x = 1, 2, 3, and 4) structures and the distance effect on the catalytic CO$_2$ reduction performance was further investigated. Combining charge density difference, electron localization function, and density of states between Fe atomic pair sites and coordination pyridine nitrogen, the four catalysts displayed good structural stability in electronic structure. Moreover, the negative E_f and positive U_{diss} indicated that the four different distance Fe atomic pairs can be stably anchored by nitrogen-containing carbon materials in thermodynamics and electrochemistry. The initial CO$_2$ adsorption and activation was the key to reflect the activity of the catalyst. The optimized adsorption geometry and Bader charge transfer displayed that the FeN$_4$-D1 structure had the best activation effect on CO$_2$ molecules. Thus, the FeN$_4$-D1

structure had good catalytic potential in the CO$_2$RR. On the basis of the free energy profile, the FeN$_4$-D1 structure exhibited better catalytic performance for the CO$_2$RR to produce CO than other catalysts in C$_1$ products. And compared with the HER side reaction, FeN$_4$-Dx structures all showed better CO$_2$RR selectivity, which further proved that Fe atomic pair catalysts had potential for application in electrocatalytic CO$_2$RR. Considering the double sites of Fe atomic pair catalysts, the C–C coupling was further calculated and analyzed. The hydrogenation of the *CO intermediate was prone to form *CHO with lower reaction free energy rather than *COH. And *CO–*CHO coupling with smaller ΔG values might be the main C–C coupling method in producing C$_2$ products. Among the four catalysts, the FeN$_4$-D1 structure had the lowest ΔG values in the C–C coupling process, which indicated that the FeN$_4$-D1 structure had good potential in reducing CO$_2$ to produce C$_2$ products. Furtherly, the free energy profile showed that the CO$_2$RR on the FeN$_4$-D1 structure was prone to form ethanol with a low ΔG value (0.34 eV) and high selectivity, which was superior to most reported catalysts. Charge density difference, PDOS, and d-band center of *CO intermediates on the four catalysts proved that the distance regulation of Fe atomic pairs enabled the FeN$_4$-D1 structure to have the best catalytic performance for the CO$_2$RR to ethanol. To sum up, the accurate distance adjustment of Fe atomic pair active sites may greatly improve the electrocatalytic CO$_2$RR performance, and the FeN$_4$-D1 structure would have broad application prospects in electrochemical energy conversion.

Conflicts of interest

The authors declare no competing financial interests in this paper.

Acknowledgements

References

1 L. Li, X. Li, Y. Sun and Y. Xie, Rational design of electrocatalytic carbon dioxide reduction for a zero-carbon network, *Chem. Soc. Rev.*, 2022, **51**, 1234–1252.

2 R. Li and D. Wang, Superiority of Dual-Atom Catalysts in Electrocatalysis: One Step Further Than Single-Atom Catalysts, *Adv. Energy Mater.*, 2022, **12**, 2103564.

3 C. Jia, K. Dastafkan, W. Ren, W. Yang and C. Zhao, Carbon-based catalysts for electrochemical CO$_2$ reduction, *Sustainable Energy Fuels*, 2019, **3**, 2890–2906.

4 Y. Xue, Y. Guo, H. Cui and Z. Zhou, Catalyst Design for Electrochemical Reduction of CO$_2$ to Multicarbon Products, *Small Methods*, 2021, **5**, e2100736.

5 X. Li, S. Xi, L. Sun, S. Dou, Z. Huang, T. Su and X. Wang, Isolated FeN_4 Sites for Efficient Electrocatalytic CO_2 Reduction, *Adv. Sci.*, 2020, **7**, 2001545.

6 X. Sun, Y. Tuo, C. Ye, C. Chen, Q. Lu, G. Li, P. Jiang, S. Chen, P. Zhu, M. Ma, J. Zhang, J. H. Bitter, D. Wang and Y. Li, Phosphorus Induced Electron Localization of Single Iron Sites for Boosted CO_2 Electroreduction Reaction, *Angew. Chem., Int. Ed.*, 2021, **60**, 23614–23618.

7 Y. Wang, H. Su, Y. He, L. Li, S. Zhu, H. Shen, P. Xie, X. Fu, G. Zhou, C. Feng, D. Zhao, F. Xiao, X. Zhu, Y. Zeng, M. Shao, S. Chen, G. Wu, J. Zeng and C. Wang, Advanced Electrocatalysts with Single-Metal-Atom Active Sites, *Chem. Rev.*, 2020, **120**, 12217–12314.

8 Y. Zhang, L. Jiao, W. Yang, C. Xie and H. L. Jiang, Rational Fabrication of Low-Coordinate Single-Atom Ni Electrocatalysts by MOFs for Highly Selective CO_2 Reduction, *Angew. Chem., Int. Ed.*, 2021, **60**, 7607–7611.

9 Q.-X. Li, D.-H. Si, W. Lin, Y.-B. Wang, H.-J. Zhu, Y.-B. Huang and R. Cao, Highly efficient electroreduction of CO_2 by defect single-atomic $Ni-N_3$ sites anchored on ordered micro-macroporous carbons, *Sci. China: Chem.*, 2022, **65**, 1584–1593.

10 D. Chen, L. H. Zhang, J. Du, H. Wang, J. Guo, J. Zhan, F. Li and F. Yu, A Tandem Strategy for Enhancing Electrochemical CO_2 Reduction Activity of Single-Atom $Cu-S_1N_3$ Catalysts via Integration with Cu Nanoclusters, *Angew. Chem., Int. Ed.*, 2021, **60**, 24022–24027.

11 S. Chen, X. Li, C. W. Kao, T. Luo, K. Chen, J. Fu, C. Ma, H. Li, M. Li, T. S. Chan and M. Liu, Unveiling Proton-feeding Effect in Sulfur-doped Fe-N-C Single-Atom Catalyst for Enhanced CO_2 Electroreduction, *Angew. Chem., Int. Ed.*, 2022, **134**, e202206233.

12 F. Pan, B. Li, E. Sarnello, S. Hwang, Y. Gang, X. Feng, X. Xiang, N. M. Adli, T. Li, D. Su, G. Wu, G. Wang and Y. Li, Boosting CO_2 reduction on Fe-N-C with sulfur incorporation: Synergistic electronic and structural engineering, *Nano Energy*, 2020, **68**, 104384.

13 H. Zhang, J. Li, S. Xi, Y. Du, X. Hai, J. Wang, H. Xu, G. Wu, J. Zhang, J. Lu and J. Wang, A Graphene-Supported Single-Atom FeN_5 Catalytic Site for Efficient Electrochemical CO_2 Reduction, *Angew. Chem., Int. Ed.*, 2019, **58**, 14871–14876.

14 X. Wang, Y. Pan, H. Ning, H. Wang, D. Guo, W. Wang, Z. Yang, Q. Zhao, B. Zhang, L. Zheng, J. Zhang and M. Wu, Hierarchically micro- and meso-porous $Fe-N_4O$-doped carbon as robust electrocatalyst for CO_2 reduction, *Appl. Catal., B*, 2020, **266**, 118630.

15 L. Lin, H. Li, C. Yan, H. Li, R. Si, M. Li, J. Xiao, G. Wang and X. Bao, Synergistic Catalysis over Iron-Nitrogen Sites Anchored with Cobalt Phthalocyanine for Efficient CO_2 Electroreduction, *Adv. Mater.*, 2019, **31**, e1903470.

16 X. Wei, S. Wei, S. Cao, S. Hu, S. Zhou, S. Liu, Z. Wang and X. Lu, Cu acting as Fe activity promoter in dual-atom Cu/Fe-NC catalyst in CO_2RR to C1 products, *Appl. Surf. Sci.*, 2021, **564**, 150423.

17 J. Zhu, M. Xiao, D. Ren, R. Gao, X. Liu, Z. Zhang, D. Luo, W. Xing, D. Su, A. Yu and Z. Chen, Quasi-Covalently

Coupled Ni-Cu Atomic Pair for Synergistic Electroreduction of CO_2, *J. Am. Chem. Soc.*, 2022, **144**, 9661–9671.

18 W. Ren, X. Tan, W. Yang, C. Jia, S. Xu, K. Wang, S. C. Smith and C. Zhao, Isolated Diatomic Ni-Fe Metal-Nitrogen Sites for Synergistic Electroreduction of CO_2, *Angew. Chem., Int. Ed.*, 2019, **58**, 6972–6976.

19 Y. Li, R. Hu, Z. Chen, X. Wan, J.-X. Shang, F.-H. Wang and J. Shui, Effect of Zn atom in Fe-N-C catalysts for electrocatalytic reactions: theoretical considerations, *Nano Res.*, 2021, **14**, 611–619.

20 Z. Jin, P. Li, Y. Meng, Z. Fang, D. Xiao and G. Yu, Understanding the inter-site distance effect in single-atom catalysts for oxygen electroreduction, *Nat. Catal.*, 2021, **4**, 615–622.

21 A. J. Garza, A. T. Bell and M. Head-Gordon, Mechanism of CO_2 Reduction at Copper Surfaces: Pathways to C_2 Products, *ACS Catal.*, 2018, **8**, 1490–1499.

22 C. Wang, C. Zhu, M. Zhang, Y. Geng and Z. Su, Copper Dimer Anchored in g-CN Monolayer as an Efficient Electrocatalyst for CO_2 Reduction Reaction: A Computational Study, *Adv. Theory Simul.*, 2020, **3**, 2000218.

23 Y. Jiao, Y. Zheng, P. Chen, M. Jaroniec and S. Z. Qiao, Molecular Scaffolding Strategy with Synergistic Active Centers To Facilitate Electrocatalytic CO_2 Reduction to Hydrocarbon/Alcohol, *J. Am. Chem. Soc.*, 2017, **139**, 18093–18100.

24 X. Su, Z. Jiang, J. Zhou, H. Liu, D. Zhou, H. Shang, X. Ni, Z. Peng, F. Yang, W. Chen, Z. Qi, D. Wang and Y. Wang, Complementary Operando Spectroscopy identification of in-situ generated metastable charge-asymmetry Cu_2-CuN_3 clusters for CO_2 reduction to ethanol, *Nat. Commun.*, 2022, **13**, 1322.

25 M. Behrens, F. Studt, I. Kasatkin, S. Kühl, M. Hävecker, F. Abild-Pedersen, S. Zander, F. Girgsdies, P. Kurr, B.-L. Kniep, M. Tovar, R. W. Fischer, J. K. Nørskov and R. Schlögl, The Active Site of Methanol Synthesis over $Cu/ZnO/Al_2O_3$ Industrial Catalysts, *Science*, 2012, **336**, 893–897.

26 J. A. Rodriguez, P. Liu, D. J. Stacchiola, S. D. Senanayake, M. G. White and J. G. Chen, Hydrogenation of CO_2 to Methanol: Importance of Metal–Oxide and Metal–Carbide Interfaces in the Activation of CO_2, *ACS Catal.*, 2015, **5**, 6696–6706.

27 K. Lakshmanan, W. H. Huang, S. A. Chala, B. W. Taklu, E. A. Moges, J. F. Lee, P. Y. Huang, Y. C. Lee, M. C. Tsai, W. N. Su and B. J. Hwang, Highly Active Oxygen Coordinated Configuration of Fe Single-Atom Catalyst toward Electrochemical Reduction of CO_2 into Multi-Carbon Products, *Adv. Funct. Mater.*, 2022, **32**, 2109310.

28 X. Liu, Z. Wang, Y. Tian and J. Zhao, Graphdiyne-Supported Single Iron Atom: A Promising Electrocatalyst for Carbon Dioxide Electroreduction into Methane and Ethanol, *J. Phys. Chem. C*, 2020, **124**, 3722–3730.

29 M. He, W. An, Y. Wang, Y. Men and S. Liu, Hybrid Metal-Boron Diatomic Site Embedded in C_2N Monolayer Promotes C-C Coupling in CO_2 Electroreduction, *Small*, 2021, **17**, 2104445.

30 S. K. Kaiser, Z. Chen, D. Faust Akl, S. Mitchell and J. Perez-Ramirez, Single-Atom Catalysts across the Periodic Table, *Chem. Rev.*, 2020, **120**, 11703–11809.

31 W. Song, X. Lv, Y. Gao and L. Wang, Photocatalytic HER Performance of TiO₂-supported Single Atom Catalyst Based on Electronic Regulation: A DFT Study, *Chem. Res. Chin. Univ.*, 2021, **38**, 1025–1031.

32 Y. Song, L. Tao, Y. Zhang, J. Pan and S. Du, A DFT Investigation on the Electronic Structures and Au Adatom Assisted Hydrogenation of Graphene Nanoflake Array, *Chem. Res. Chin. Univ.*, 2021, **37**, 1110–1115.

33 G. Kresse and J. Furthmüller, Efficient iterative schemes for ab initio total-energy calculations using a plane-wave basis set, *Phys. Rev. B: Condens. Matter Mater. Phys.*, 1996, **54**, 11169.

34 J. P. Perdew, K. Burke and M. Ernzerhof, Generalized gradient approximation made simple, *Phys. Rev. Lett.*, 1996, **77**, 3865.

35 H. J. Monkhorst and J. D. Pack, Special points for Brillouin-zone integrations, *Phys. Rev. B: Condens. Matter Mater. Phys.*, 1976, **13**, 5188–5192.

36 K. Mathew, R. Sundararaman, K. Letchworth-Weaver, T. A. Arias and R. G. Hennig, Implicit solvation model for density-functional study of nanocrystal surfaces and reaction pathways, *J. Chem. Phys.*, 2014, **140**, 084106.

37 Y. Yuan, X. Gong and H. Wang, The synergistic mechanism of graphene and MoS₂ for hydrogen generation: insights from density functional theory, *Phys. Chem. Chem. Phys.*, 2015, **17**, 11375–11381.

38 J. K. Nørskov, J. Rossmeisl, A. Logadottir, L. Lindqvist, J. R. Kitchin, T. Bligaard and H. Jonsson, Origin of the overpotential for oxygen reduction at a fuel-cell cathode, *J. Phys. Chem. B*, 2004, **108**, 17886–17892.

39 V. Wang, N. Xu, J.-C. Liu, G. Tang and W.-T. Geng, VASPKIT: A user-friendly interface facilitating high-throughput computing and analysis using VASP code, *Comput. Phys. Commun.*, 2021, **267**, 108033.

40 F. Abild-Pedersen, J. Greeley, F. Studt, J. Rossmeisl, T. R. Munter, P. G. Moses, E. Skulason, T. Bligaard and J. K. Norskov, Scaling properties of adsorption energies for hydrogen-containing molecules on transition-metal surfaces, *Phys. Rev. Lett.*, 2007, **99**, 016105.

41 H. Wu and F. He, Activity Origins of Graphdiyne Based Bifunctional Atom Catalysts for Hydrogen Evolution and Water Oxidation, *Chem. Res. Chin. Univ.*, 2021, **37**, 1334–1340.

42 G. Zhu, Y. Li, H. Zhu, H. Su, S. H. Chan and Q. Sun, Curvature-Dependent Selectivity of CO₂ Electrocatalytic Reduction on Cobalt Porphyrin Nanotubes, *ACS Catal.*, 2016, **6**, 6294–6301.

43 D. Jiao, Y.-j Liu, Q. Cai and J.-X. Zhao, Coordination Tunes Activity and Selectivity of Nitrogen Reduction Reaction on Single-Atom Iron Catalysts: A Computational Study, *J. Mater. Chem. A*, 2020, **9**, 1240–1251.

44 T. G. Senthamaraikannan and D.-H. Lim, CO₂ Reduction to C₁ and C₂ Compounds on Sulfur-Deficient Mackinawite (FeS): A Density Functional Theory Study, *J. Phys. Chem. C*, 2022, **126**, 7012–7021.

45 S. Chen, H. Yuan, S. I. Morozov, L. Ge, L. Li, L. Xu and W. A. Goddard, 3rd, Design of a Graphene Nitrene Two-Dimensional Catalyst Heterostructure Providing a Well-Defined Site Accommodating One to Three Metals, with Application to CO₂ Reduction Electrocatalysis for the Two-Metal Case, *J. Phys. Chem. Lett.*, 2020, **11**, 2541–2549.

46 Y. Zhao, S. Zhou and J. Zhao, Selective C–C Coupling by Spatially Confined Dimeric Metal Centers, *iScience*, 2020, **23**, 101051.

47 X. Bai, Q. Li, L. Shi, X. Niu, C. Ling and J. Wang, Hybrid Cu⁰ and Cuˣ⁺ as Atomic Interfaces Promote High-Selectivity Conversion of CO₂ to C₂H₅OH at Low Potential, *Small*, 2020, **16**, e1901981.

48 J.-S. Wang, G.-C. Zhao, Y.-Q. Qiu and C.-G. Liu, Strong Boron–Carbon Bonding Interaction Drives CO₂ Reduction to Ethanol over the Boron-Doped Cu(111) Surface: An Insight from the First-Principles Calculations, *J. Phys. Chem. C*, 2020, **125**, 572–582.

49 Q. Yang, X. Liu, W. Peng, Y. Zhao, Z. Liu, M. Peng, Y.-R. Lu, T.-S. Chan, X. Xu and Y. Tan, Vanadium Oxide Integrated on Hierarchically Nanoporous Copper for Efficient Electro-reduction of CO₂ to Ethanol, *J. Mater. Chem. A*, 2021, **9**, 3044–3051.

50 S. Sun, X. Zhou, B. Cong, W. Hong and G. Chen, Tailoring the d-Band Centers Endows (NiₓFe₁₋ₓ)₂P Nanosheets with Efficient Oxygen Evolution Catalysis, *ACS Catal.*, 2020, **10**, 9086–9097.